





Bifurcation of excited state trajectories toward energy transfer or electron transfer directed by wave function symmetry

Paola S. Oviedo^{a,b}, Luis M. Baraldo^{a,b,1} , and Alejandro Cadranel^{a,b,c,1} 

^aDepartamento de Química Inorgánica, Analítica y Química Física, Facultad de Ciencias Exactas y Naturales, Universidad de Buenos Aires, C1428EHA Buenos Aires, Argentina; ^bInstituto de Química Física de Materiales, Medio Ambiente y Energía, CONICET, Universidad de Buenos Aires, C1428EHA Buenos Aires, Argentina; and ^cInterdisciplinary Center for Molecular Materials, Department of Chemistry and Pharmacy, Friedrich-Alexander Universität Erlangen-Nürnberg, 91058 Erlangen, Germany

Edited by Michael R. Wasielewski, Northwestern University, Evanston, IL, and accepted by Editorial Board Member Catherine J. Murphy December 10, 2020 (received for review September 2, 2020)

This work explores the concept that differential wave function overlap between excited states can be engineered within a molecular chromophore. The aim is to control excited state wave function symmetries, so that symmetry matches or mismatches result in differential orbital overlap and define low-energy trajectories or kinetic barriers within the excited state surface, that drive excited state population toward different reaction pathways. Two donor–acceptor assemblies were explored, where visible light absorption prepares excited states of different wave function symmetry. These states could be resolved using transient absorption spectroscopy, thanks to wave function symmetry-specific photoinduced optical transitions. One of these excited states undergoes energy transfer to the acceptor, while another undertakes a back-electron transfer to restate the ground state. This differential behavior is possible thanks to the presence of kinetic barriers that prevent excited state equilibration. This strategy can be exploited to avoid energy dissipation in energy conversion or photoredox catalytic schemes.

wave function symmetry | excited state electronic coupling | photoinduced mixed valence | energy transfer | electron transfer

In the late 1960s, after analyzing many examples of textbook organic chemical reactions, Woodward and Hoffman postulated that any concerted chemical reaction must proceed with orbital symmetry conservation (1, 2), and later, Eaton extended this concept to transition metal complexes (3). Correlation diagrams were used to interpret that the symmetry of the transition states dictates the product selectivity. Years later, the influence of symmetry on the simplest chemical reactions, i.e., energy/electron transfer, has been studied by comparing different (supra)molecular systems. These systems usually include the same electron donor–acceptor pairs, and variations are made using bridges of diverse geometries to connect them. This allowed the systems to span several donor–acceptor relative orientations, encompassing, thus, cases where donor and acceptor wave function symmetries match or mismatch, without modifying the underlying energetics (4–10).

In a prominent example, nature itself relies on wave function symmetry to control the directionality of the electron transfer flow in the respiratory chain of *Thermus thermophilus*. It has been proposed that a conformational change of a redox mediator copper site triggers a switch of its ground state wave function symmetry, from that one matching with a donor to that one matching with an acceptor (11). However, despite more than 50 y of electron and energy transfer research, we found very few examples where the same molecular system or interface undergoes different reaction pathways depending on wave function properties. Different rates for electron transfer from small molecules to gold surfaces were observed when different molecular orbitals were populated (12). Also, orbital-specific optical electron transfer

transitions were resolved in cyanide-bridged {Os^{II}-Ru^{III}} mixed valence systems by means of electronic Stark spectroscopy (13). Furthermore, orbital-specific dipolar energy transfer was demonstrated in supramolecular {Re-Co} assemblies (14). Additionally, the influence of quantum interference and orbital symmetry were theoretically shown to result in several distinct exchange energy transfer pathways within the same donor–acceptor system (15).

In a very recent report, oppositely polarized charge transfer excited states within the same chromophore were manipulated to preferentially access high-energy excited states (16). This was based on differential spatial wave function overlap, mainly controlled by donor–acceptor distances. We are also working on the concept that differential wave function overlap between excited states can be engineered within a molecular chromophore. However, instead of controlling donor–acceptor distances, our strategy is based on controlling wave function symmetries (17), so that symmetry matches or mismatches help in driving the excited state trajectories. To achieve this, probe systems should be rigid and hold fixed donor–acceptor orientations, for which cyanide-bridged multimetallic assemblies are ideal candidates (18–22). In this contribution, we explore two donor–acceptor assemblies, namely, [Ru(tpy)(bpy)(μCN)Ru(py)₄(μNC)Cr(CN)₅] (RuRuCr) and [Ru(tpy)(bpy)(μNC)Cr(CN)₅][−] (RuCr[−]) (Fig. 1), where visible light absorption prepares ruthenium-centered MLCT excited states of different wave function symmetry. Nanosecond and femtosecond transient absorption spectroscopies

Significance

Electron transfer and energy transfer are the simplest chemical reactions and the key processes involved in cellular respiration, energy conversion schemes like photosynthesis, and photoredox catalysis. In photoreactive systems, any decay cascade to lower excited states that precedes electron or energy transfer dissipates part of the energy absorbed from light. Our findings show that influence of symmetry on energy or electron transfer, related to orbital overlap, can be exploited to avoid detrimental energy losses, decisive for improving energy conversion and expanding the limits of photoredox catalysis.

Author contributions: A.C. designed research; P.S.O. and A.C. performed research; P.S.O., L.M.B., and A.C. analyzed data; and L.M.B. and A.C. wrote the paper.

The authors declare no competing interest.

This article is a PNAS Direct Submission. M.R.W. is a guest editor invited by the Editorial Board.

Published under the PNAS license.

¹To whom correspondence may be addressed. Email: baraldo@qi.fcen.uba.ar or acadranel@qi.fcen.uba.ar.

This article contains supporting information online at <https://www.pnas.org/lookup/suppl/doi:10.1073/pnas.2018521118/-DCSupplemental>.

Published January 18, 2021.

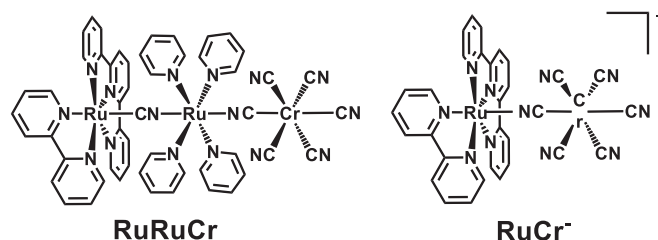


Fig. 1. Sketches of the complexes studied in this work.

(nsTAS and fsTAS, respectively) revealed that one of these states readily engages in exchange energy transfer to the chromium acceptor, while another one undergoes back-electron transfer to restate the ground state in a much slower timescale. Since the photogenerated MLCT states are not equilibrated in the analyzed timescale, this strategy can be used to avoid energy dissipation in energy conversion or photoredox catalytic schemes.

Results

The UV-vis-NIR absorption profiles of RuRuCr and RuCr⁻ in DMSO are shown in the *SI Appendix, Fig. S1*, and those of their one electron oxidized species RuRuCr⁺ and RuCr and one electron reduced species RuRuCr⁻ and RuCr²⁻, are displayed in the *SI Appendix, Fig. S2*. For RuRuCr, the absorption spectrum is governed by MLCT transitions at 27,300 and 21,500 cm⁻¹, centered on the {Ru(py)₄} and {Ru(tpy)(bpy)} fragments, respectively (23). The first one electron oxidation occurs on {Ru(py)₄}, and this results in a significant decrease of the high-energy band, with a smaller effect on the low-energy band. Importantly, RuRuCr⁺ contains a (dπ⁶)-(dπ⁵) mixed valence {RuRu} core that gives rise to a broad ground state intervalence charge transfer (GSIVCT) absorption that extends to the NIR and peaks below 10,000 cm⁻¹ (*SI Appendix, Fig. S2, Inset*). On the other hand, one electron reduction affords a tpy^{•-} radical anion, with spectral features at 27,200 and 19,300 cm⁻¹ and weak and broad transitions to the red. For RuCr⁻, {Ru(tpy)(bpy)} MLCT absorptions dominate at 20,900 cm⁻¹, and they disappear for RuCr due to chromophore oxidation. The absence of a mixed valence system in RuCr makes it NIR silent. RuCr²⁻ presents the features of the tpy^{•-} radical anion. Photoexcitation in the MLCT manifold of RuRuCr and RuCr⁻ in DMSO at room temperature triggers energy transfer processes to the {Cr(CN)₆} acceptor, affording microsecond-lived chromium-centered emissive ²E states. However, in both cases, ruthenium-centered ³MLCT emission is also discernable, although with very weak intensity (23). To shed light on the excited state dynamics behind this complex behavior, nsTAS experiments using vis-NIR detection were performed. RuRuCr was excited into the MLCT manifold at 25,800 cm⁻¹ (387 nm), in DMSO at room temperature. Differential spectra at selected time delays are presented in *SI Appendix, Fig. S3*, and the complete set is shown as a three-dimensional (3D) map in Fig. 2. In the first 10 ns, the evolution of the time absorption traces shows a slight increase between 21,000 and 22,000 cm⁻¹ and a noticeable decrease between 13,000 and 19,000 cm⁻¹ (*SI Appendix, Fig. S3*). At longer time delays, a spectrum with two maxima at 21,050 and 15,400 cm⁻¹ can be observed, that monotonically decays to zero. Inspection of the kinetic trace at 15,400 cm⁻¹ (Fig. 2) confirms differential absorption changes in two different time scales. This suggests that two species with different lifetimes are detected in this experiment, consistent with the dual ³MLCT-²E emission observed in steady-state measurements. A multiwavelength global analysis of the nsTAS data reveals two decay lifetimes, one under 10 ns and the other one in the microsecond range (*SI Appendix, Table S1*). A target analysis (24–26) with two parallel, independently decaying

species was followed to model the excited state decays, and the resulting species-associated differential spectra are shown in Fig. 2. One of these excited states decays in 13.1 μs to the ground state, and we assign it to the chromium-centered ²E(Cr) state (black curve in Fig. 2). This differential spectrum presents two maxima, at 21,050 and 15,400 cm⁻¹ (475 and 650 nm). This pattern is ascribed to excited-state intervalence charge transfers, from the ruthenium(II) ions to the excited chromium(III), and resembles that one observed for ²E states in related cyanide-bridged {Cr-Ru-Cr} multimetallic complexes (27–29). The other excited state (red curve in Fig. 2) deactivates restating the ground state in 4.4 ns, and its differential absorption spectrum includes features of an oxidized ruthenium ion and also those of the tpy^{•-} radical anion (*SI Appendix, Fig. S2*). These are typical differential features of {Ru(tpy)(bpy)}-centered MLCT states of monometallic complexes, such as [Ru(tpy)(bpy)(CN)]⁺ (17). It involves a minimum at 21,100 cm⁻¹ and weak and broad photoinduced absorptions to the red. The decay of this state is responsible for the transient absorption changes observed during the first few nanoseconds (*SI Appendix, Fig. S3*). This differential spectrum lacks any strong photoinduced absorptions in the NIR, which are usually associated with photoinduced intervalence charge transfers (PIIVCT) as observed in other multimetallic assemblies (30). We assign this absence to the orientation of the ruthenium dπ(t_{2g}) orbital bearing the excited hole in this MLCT excited state, that is orthogonal to the intermetallic z axis (17, 31). Therefore, this differential spectrum is ascribed to a ³MLCT_{xy} state with an {Ru^{III}(tpy^{•-})(bpy)(μCN)Ru^{II}(py)₄} electronic configuration.

nsTAS experiments on RuCr⁻ in DMSO at room temperature follow a similar course. In this case, 19,800 cm⁻¹ (505 nm) excitation was used due to the low extinction coefficient of RuCr⁻ at 25,800 cm⁻¹. *SI Appendix, Fig. S4*, shows transient spectra at selected time delays, and *SI Appendix, Fig. S5*, shows the complete set as a 3D map. Two exponential processes are observed in the kinetic trace at 21,050 cm⁻¹ (*SI Appendix, Fig. S5*), resembling the kinetic behavior observed upon photoexcitation of RuRuCr. Similarly, we assign this behavior as two excited states that decay independently to the ground state. Target analysis reveals lifetimes of 17.4 μs and 8 ns, respectively (*SI Appendix, Table S1*). The former is assigned to the chromium centered ²E(Cr), whose differential spectrum presents maxima at 18,900 and 17,200 cm⁻¹ (black curve in *SI Appendix, Fig. S5*), and the latter is assigned to a ³MLCT, associated with a negative signal that mirrors ground state absorption and broad and weak signals to the red (red curve in *SI Appendix, Fig. S5*). This pattern also is the result of additive contributions from the differential spectra obtained upon one electron oxidation and reduction (*SI Appendix, Fig. S2*). This is consistent with the dual ³MLCT-²E emission observed in steady-state measurements RuCr⁻ as well. Please note that the chromophoric donor {Ru(tpy)(bpy)} in RuCr⁻ is monometallic, and hence, the absence of a PIIVCT band cannot be used to assign the wave function symmetry of the ³MLCT. However, it presents a very similar kinetic behavior as the ³MLCT_{xy} state in RuRuCr. Thus, we also assign it as a ³MLCT_{xy} with a {Ru^{III}(tpy^{•-})} configuration and a hole orientation orthogonal to the intermetallic axis.

To gain a deeper insight into the excited state behavior before and during the energy transfer process, we turned to fsTAS measurements on RuRuCr in DMSO at room temperature, using 25,800 cm⁻¹ (387 nm) excitation into the MLCT manifold. *SI Appendix, Fig. S6*, shows selected data at different delay times, and the complete set is presented as a 3D map in Fig. 3. Since the first picoseconds, a bleach below 19,000 cm⁻¹ and an intense positive signal around 6,900 cm⁻¹ are observed. The former indicates the loss of ground state population upon photoexcitation. The latter corresponds to a PIIVCT within the {RuRu} moiety in the photoexcited trimetallic complex and indicates strong metal-metal electronic communication (30). Importantly, previous

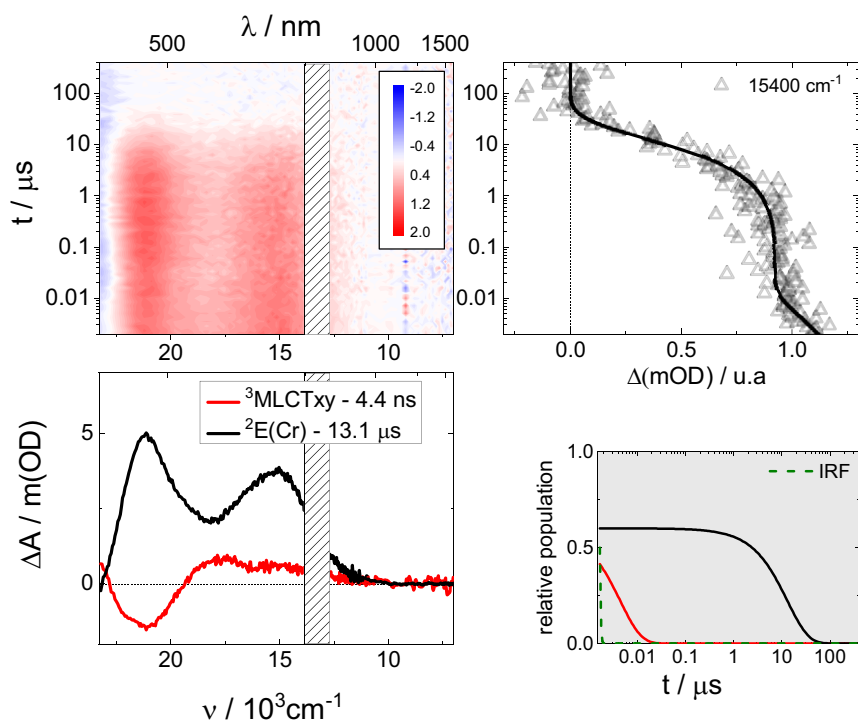


Fig. 2. Nanosecond transient absorption spectroscopy. Differential absorption 3D map obtained from nsTAS with $25,800\text{ cm}^{-1}$ (387 nm) excitation of RuRuCr in DMSO at room temperature (*Upper Left*). Species associated differential spectra of $^3\text{MLCTxy}$ and $^2\text{E}(\text{Cr})$ (*Bottom Left*). Differential absorption kinetic trace at $15,400\text{ cm}^{-1}$ (*Upper Right*) and relative populations of $^3\text{MLCTxy}$ and $^2\text{E}(\text{Cr})$ (*Bottom Right*).

experiments and theoretical calculations with the $[\text{Ru}(\text{tpy})(\text{bpy})(\mu\text{CN})\text{Ru}(\text{py})_4\text{Cl}]^{2+}$ model system prove the electronic origins of this NIR band. The kinetic trace at $6,900\text{ cm}^{-1}$ displays a monoexponential decay with a time constant close to 100 ps (Fig. 3). At 3 ns this band

has disappeared (*SI Appendix, Fig. S6*), and the spectrum shows a completely different pattern that includes photoinduced absorptions at $21,050\text{ cm}^{-1}$ and $15,400\text{ cm}^{-1}$. This spectral profile resembles the microsecond transient absorption spectra, and therefore, we

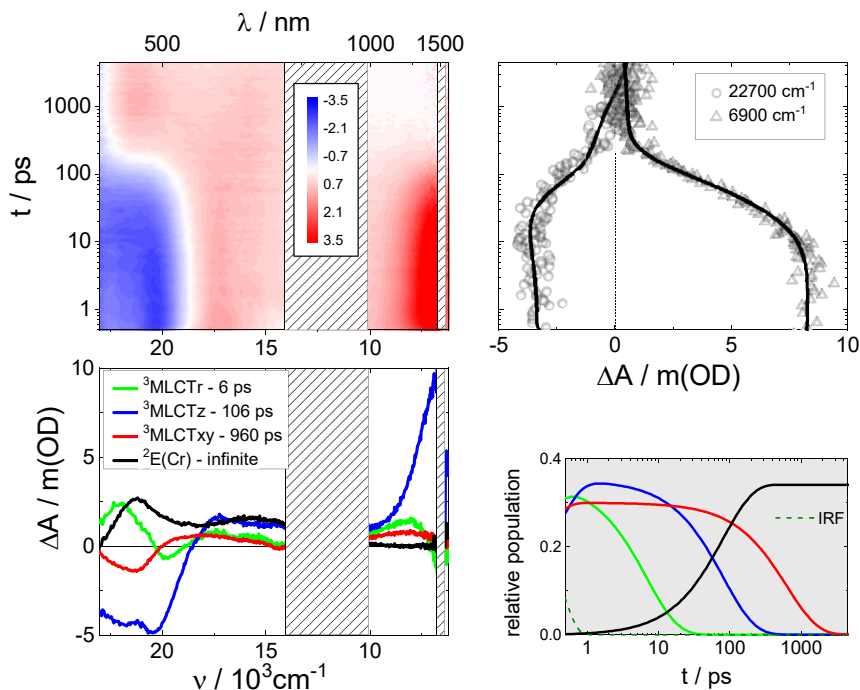


Fig. 3. Femtosecond transient absorption spectroscopy. Differential absorption 3D map obtained from fsTAS with $25,800\text{ cm}^{-1}$ (387 nm) excitation of RuRuCr in DMSO at room temperature (*Upper Left*). Species associated differential spectra of $^3\text{MLCTr}$, $^3\text{MLCTz}$, $^3\text{MLCTxy}$, and $^2\text{E}(\text{Cr})$ (*Bottom Left*). Differential absorption kinetic traces at $6,900$ and $22,700\text{ cm}^{-1}$ (*Upper Right*) and relative populations of $^3\text{MLCTr}$, $^3\text{MLCTz}$, $^3\text{MLCTxy}$, and $^2\text{E}(\text{Cr})$ (*Bottom Right*).

attribute this process to the energy transfer process that feeds the chromium centered ${}^2\text{E}(\text{Cr})$.

The kinetic trace at $22,700\text{ cm}^{-1}$ (Fig. 3), instead, reveals the presence of several processes. A multiwavelength global analysis of the fsTAS data rendered three exponential processes and an infinite offset (SI Appendix, Table S1). Therefore, a complex model was required. We applied the target model depicted in Fig. 4 to fit the data, which is similar to that previously applied to the $[\text{Ru}(\text{tpy})(\text{bpy})(\mu\text{CN})\text{Ru}(\text{py})_4\text{Cl}]^{2+}$ model system (17) but includes an energy transfer to the microsecond living ${}^2\text{E}(\text{Cr})$ state. The resulting species-associated differential spectra are shown in Fig. 3. Our observations start after intersystem crossing from the singlet to the triplet MLCT manifold has taken place (32). At the beginning of the experiment, three different excited states with different spectral signatures are populated, which evolve parallelly with time. One of them has a differential spectrum with a minimum at $21,300\text{ cm}^{-1}$, broad and weak photoinduced absorptions to the red, but no NIR absorptions. These features agree with those of ${}^3\text{MLCT}_{xy}$ population (red curve, Fig. 3). It decays to the ground state in 960 ps. This lifetime is somehow shorter than that obtained in nsTAS experiments, but it is still consistent considering the complexity of the model applied. Another of the initially populated excited states is a very short lived excited state, and its differential absorption profile (green curve in Fig. 3) coincides with that assigned to an excited state with a remote $\{\text{Ru}^{\text{II}}(\text{tpy}^*)(\text{bpy})(\mu\text{CN})\text{Ru}^{\text{III}}(\text{py})_4\}$ electronic configuration observed following photoexcitation of $[\text{Ru}(\text{tpy})(\text{bpy})(\mu\text{CN})\text{Ru}(\text{py})_4\text{Cl}]^{2+}$ (17). It is labeled as ${}^3\text{MLCT}_z$, which is also NIR silent and decays to the ground state in 6 ps, probably due to the thermal population of ${}^3\text{LF}$ states of the $\{\text{Ru}(\text{py})_4\}$ moiety (33). The third, initially populated excited state presents negative signals corresponding to the bleached ground-state MLCT absorptions at $20,400\text{ cm}^{-1}$ and an intense PIIVCT at $6,900\text{ cm}^{-1}$ (blue curve in Fig. 3). The strong NIR activity is an indication of a photoinduced $d\pi^5-d\pi^6$ mixed-valence system, which implies that the ruthenium $d\pi(t_{2g})$ orbitals bearing the excited hole are delocalized over the entire $\{\text{RuRu}\}$ moiety and that the wave function symmetry is parallel to the intermetallic z axis. Therefore, we assign this state as ${}^3\text{MLCT}_z$. Its decay can be followed by the decrease of the absorption at $6,900\text{ cm}^{-1}$, and it is concomitant with the rise of the chromium-centered

${}^2\text{E}(\text{Cr})$ excited state signatures at $21,100$ and $15,700\text{ cm}^{-1}$ (black curve in Fig. 3). This process is the energy transfer, which takes 106 ps, in accordance with the previously reported value (23). Similar experiments on RuRuCr under $19,800\text{ cm}^{-1}$ (505 nm) excitation in DMSO at room temperature were performed (SI Appendix, Fig. S7). These allow us to primarily excite $\{\text{Ru}(\text{tpy})(\text{bpy})\}$ -based MLCT states, rather than $\{\text{Ru}(\text{py})_4\}$ -based MLCTs. The results are analogous to those under $25,800\text{ cm}^{-1}$ (387 nm) excitation, with the exception that the ${}^3\text{MLCT}_r$ state is not observed (SI Appendix, Fig. S8).

fsTAS experiments on RuCr⁻ under $19,800\text{ cm}^{-1}$ (505 nm) excitation in DMSO at room temperature can also be understood with a similar mechanism. Upon excitation, the typical MLCT features are observed, including a negative signal mirroring ground state absorption and weak and broad signals to the red (SI Appendix, Figs. S9 and S10). At 20 ps, these signatures have evolved to a differential profile matching that of ${}^2\text{E}(\text{Cr})$. Also, kinetic traces at $22,800$ and $16,800\text{ cm}^{-1}$ show excited state activity before 20 ps but negligible changes afterward (SI Appendix, Fig. S10). Global analysis reveals one exponential process with a time constant of 5.2 ps and an infinite offset in this timescale (SI Appendix, Table S1), and the corresponding associated differential spectra are shown in SI Appendix, Fig. S8. We assign the initially populated excited state as ${}^3\text{MLCT}_z$ (blue curve in SI Appendix, Fig. S10) by analogy with the proposed model for the decay of RuRuCr. It readily transfers the electronic energy to ${}^2\text{E}(\text{Cr})$ in 5.2 ps, matching the previously reported value (23). The model is depicted in SI Appendix, Fig. S11. Unfortunately, we were not able to separately resolve the ${}^2\text{E}(\text{Cr})$ and ${}^3\text{MLCT}_{xy}$ components in this case, because both have lifetimes longer than the resolution of our fsTAS experiment, so the black curve in SI Appendix, Fig. S8, is mainly the differential spectrum of ${}^2\text{E}(\text{Cr})$ with minor contributions from that of ${}^3\text{MLCT}_{xy}$.

Discussion

The evolution of the NIR absorption at $6,900\text{ cm}^{-1}$ for RuRuCr allows us to follow without interference the decay of the excited state bearing this unique signal. We assign this band as a PIIVCT and this state as ${}^3\text{MLCT}_z$, a mixed valence system where the hole is located on an orbital delocalized over the entire $\{\text{RuRu}\}$ moiety and parallel to the intermetallic z axis. In these photoinduced

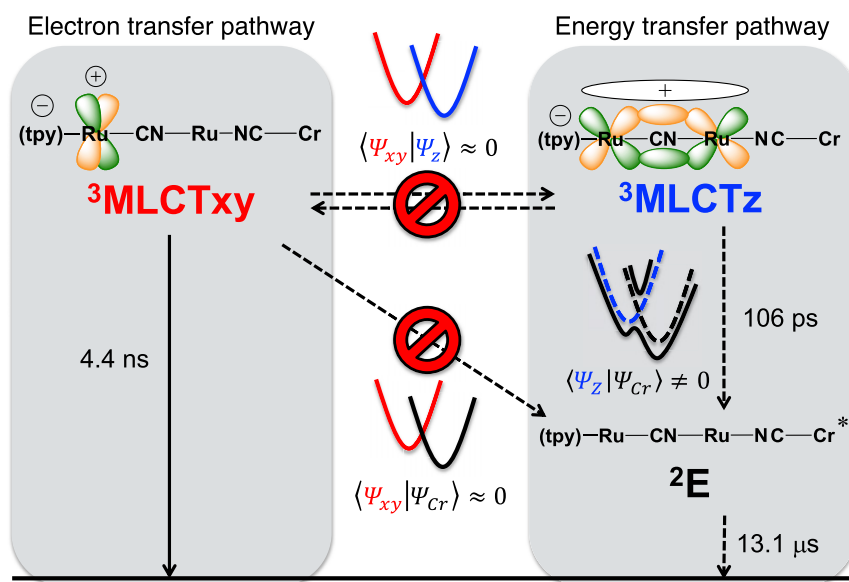


Fig. 4. Target model applied to fit the transient absorption data, considering separate electron transfer and energy transfer pathways for RuRuCr. Electronic coupling between states of different wave function symmetry is small and results in two separate reaction pathways.

mixed valence interactions, $\{\text{Ru}(\text{py})_4\}$ is the donor moiety, and $\{\text{Ru}(\text{tpy})\}$ is the acceptor, as in related model systems (17, 31). The donor–acceptor roles are reversed with respect to the ground state, as a result of the presence of the $\text{tpy}^{\cdot-}$ radical anion (30). ${}^3\text{MLCTz}$ is responsible of the energy transfer process as it clearly feeds the ${}^2\text{E}(\text{Cr})$ state with a lifetime of 106 ps.

A pivotal aspect of our target models for RuRuCr and RuCr[−] is whether the ${}^3\text{MLCTxy}$ states decay feeding ${}^2\text{E}(\text{Cr})$ or not. If a sequential model is applied to fit the nsTAS data, i.e., a model where ${}^3\text{MLCTxy}$ states feed ${}^2\text{E}(\text{Cr})$, two differential spectra very similar to each other and to that of ${}^2\text{E}(\text{Cr})$ are obtained, both for RuRuCr (*SI Appendix, Fig. S12*) and for RuCr[−] (*SI Appendix, Fig. S13*). This lacks any physicochemical meaning, considering the well-known excited state behavior of $\{\text{Cr}(\text{CN})_6\}$ (27, 34–36), and is a strong indication that two parallel, noncommunicating states are participating in the decay cascade. Additionally, ${}^3\text{MLCTxy}$ lifetimes in RuRuCr (4.4 ns) and RuCr[−] (8.3 ns) are not significantly different from those in the reference complexes $[\text{Ru}(\text{tpy})(\text{bpy})(\mu\text{CN})\text{Ru}(\text{py})_4\text{Cl}]^{2+}$ (6.3 ns) and $[\text{Ru}(\text{tpy})(\text{bpy})(\text{CN})]^+$ (13.4 ns), that bear the same donor core without any energy acceptor (17). ${}^3\text{MLCTxy}$ lifetimes are, instead, very different from ${}^3\text{MLCTz}$ lifetimes (106 ps for RuRuCr and 5.2 ps for RuCr[−]). Thus, we can conclude that ${}^3\text{MLCTxy} \rightarrow {}^2\text{E}(\text{Cr})$ energy transfer is not significantly operative.

Photolytic decomposition leading to $\{\text{Ru}(\text{tpy})(\text{bpy})(\text{solvent})\}$ species could eventually be the origin of the signals assigned here to ${}^3\text{MLCTxy}$ states. To explore this issue, RuRuCr and RuCr[−] were irradiated at 450 nm for 4 h in DMSO at room temperature, affording minimal changes in the absorption spectrum and very low photodecomposition quantum yields (*SI Appendix, Fig. S14*). Moreover, complementary nsTAS/fsTAS experiments on RuCr[−] in water at room temperature yield a ${}^3\text{MLCTxy}$ lifetime of 950 ps (*SI Appendix, Figs. S15 and S16 and Table S1*). This is one order of magnitude longer than the reported 120-ps MLCT lifetime of $[\text{Ru}(\text{tpy})(\text{bpy})(\text{OH}_2)]^{2+}$ (37), definitively supporting our assignment. Unfortunately, analogous experiments with RuRuCr in water could not be performed due to solubility reasons. Additionally, small amounts of precursor material impurities have also been considered as the origin of the signals assigned as ${}^3\text{MLCTxy}$ states. For example, $[\text{Ru}(\text{tpy})(\text{bpy})(\text{CN})]^+$ is a synthetic precursor of RuRuCr (23). Based on the spectral shapes and lifetimes of the transient signals, MLCT states in this monometallic complex behave, in fact, similar to ${}^3\text{MLCTxy}$ in RuRuCr (38). However, definitive proof of the genuineness of our assignment comes from electrochemical measurements, which are known to be much more sensitive to the presence of impurities than transient absorption. In this work, spectroscopic measurements have been performed on crystalline samples of RuRuCr, which show clean electrochemistry (23). Furthermore, detection of ${}^3\text{MLCTxy}$ in the analogous RuCr[−], with very similar spectral shape and lifetime to that of ${}^3\text{MLCTxy}$ in RuRuCr, provides further evidence supporting our rationale. In that case, the ruthenium-based precursor is not $[\text{Ru}(\text{tpy})(\text{bpy})(\text{CN})]^+$ but $[\text{Ru}(\text{tpy})(\text{bpy})\text{Cl}]^+$ instead (39). The chlorido-complex is so weakly emissive that emission quantum yield measurements are impossible (40). Therefore, residual emission signals from small amounts of this complex can be safely ruled out as the origin of dual emission or the ${}^3\text{MLCTxy}$ in RuCr[−]. Furthermore, reductive spectroelectrochemistry on RuCr[−] (*SI Appendix, Fig. S2*) shows clear isosbestic points. This is strong evidence on the absence of any other $\{\text{Ru}(\text{tpy})(\text{bpy})\}$ complexes, that, if present, would be subject of electrochemical reduction at very similar potentials and would therefore break isosbestic points.

Taking our results into concert, we can safely conclude that ${}^3\text{MLCTxy}$ is inert toward the $\{\text{Cr}(\text{CN})_6\}$ energy acceptor in RuRuCr and RuCr[−] and that back-electron transfer leading to ground state recovery is the only operative reaction pathway for ${}^3\text{MLCTxy}$. This can be rationalized in terms of Dexter theory (41). The donor–acceptor orbital overlap required for exchange energy transfer is negligible for ${}^3\text{MLCTxy}$. In this excited state,

located in the $\{\text{Ru}(\text{tpy})(\text{bpy})\}$ fragment, the hole is perpendicular to the intermetallic axis, precluding an efficient overlap with the metallic orbitals of the $\{\text{Cr}(\text{CN})_6\}$ acceptor that correspond to the octahedral t_{2g} (d_{xz} or d_{yz}). However, in ${}^3\text{MLCTz}$ the hole resides in an orbital parallel to the intermetallic axis. This allows for an effective overlap with acceptor orbitals and opens an energy transfer reactive pathway. The ${}^3\text{MLCTz} \rightarrow {}^2\text{E}(\text{Cr})$ time constant is higher for RuCr[−] than for RuRuCr because in the latter the donor orbitals are delocalized over the $\{\text{RuRu}\}$ core and therefore the overlap with the acceptor is smaller. In contrast, rationalization of the ${}^3\text{MLCTz} \rightarrow {}^2\text{E}(\text{Cr})$ energy transfer under a Förster mechanism seems difficult. Emission of the donor MLCT states occurs from 15,400 to 14,300 cm^{-1} (600 to 700 nm), while $\{\text{Cr}(\text{CN})_6\}$ absorption is close to 13,000 cm^{-1} (very close to the emission energy since ligand field transitions are not expected to undergo significant Stokes shifts), and it is spin forbidden, with an extinction coefficient below 0.4 $\text{M}^{-1} \text{cm}^{-1}$ (42). This renders a negligible spectral overlap, required for the dipolar energy transfer to occur (43). Additionally, while ${}^3\text{MLCTz}$ and ${}^3\text{MLCTxy}$ may present slightly different energies or transition dipole moments, these differences seem too small, especially in the case of RuCr[−], to account for the despair reactivity of ${}^3\text{MLCTz}$ and ${}^3\text{MLCTxy}$.

We would like to stress that it is not inherent of ${}^3\text{MLCTz}$ and ${}^3\text{MLCTxy}$ to have separate fates. In fact, in the model compound $[\text{Ru}(\text{tpy})(\text{bpy})(\text{CN})\text{Ru}(\text{py})_4\text{Cl}]^{2+}$ where there is no energy acceptor, ${}^3\text{MLCTxy}$ and ${}^3\text{MLCTz}$ have the same fate, i.e., both undergo back-electron transfer to restate the ground state. It is only in the presence of a symmetry-selective Dexter energy acceptor such as $\{\text{Cr}(\text{CN})_6\}$ that ${}^3\text{MLCTxy}$ and ${}^3\text{MLCTz}$ populations follow different pathways. The selectiveness is originated in the requirement of efficient donor–acceptor orbital overlap for electron exchange interactions to take place. In other words, efficient orbital overlap allows for exchange interactions that define a low-energy Dexter energy transfer pathway from ${}^3\text{MLCTz}$ to the acceptor. Poor donor–acceptor orbital overlap hampers exchange interactions, resulting in an obstacle for the Dexter pathway starting from ${}^3\text{MLCTxy}$. This shows how wave function symmetry impacts excited state trajectories related to electron exchange-mediated reactivity. Additionally, it should be kept in mind that for wave function symmetry to dictate the fate of the excited states, it is a prerequisite that these excited states are isolated one from another, this is, that the barriers mediating their interconversion are high, in the absence of an energy acceptor. That is exactly the photophysical scenario in the model compound $[\text{Ru}(\text{tpy})(\text{bpy})(\text{CN})\text{Ru}(\text{py})_4\text{Cl}]^{2+}$, where excited states of different wave function symmetry are observed to coexist up to the nano-second timescale (17). Thus, precise control of excited state populations and reaction pathways requires us not only to engineer wave function symmetries but also to identify and synthetically tailor the electronic factors governing interconversion between excited states. In particular, the spectroscopy of ${}^3\text{MLCTz}$ and ${}^3\text{MLCTxy}$ undoubtedly shows that they bear the excited hole in molecular orbitals with different wave function symmetry. Wave function symmetry-specific transitions, such as the PIIVCT in RuRuCr, allow for the spectroscopic resolution of both states.

However, differential orbital overlap within each excited state has another very important consequence. The positive charge density (i.e., the excited hole) in ${}^3\text{MLCTz}$ involves different fragments of the molecule than in ${}^3\text{MLCTxy}$. From this point of view, interconversion of ${}^3\text{MLCTz}$ and ${}^3\text{MLCTxy}$ can be regarded as an electron transfer reaction, where reorganization energy (both internal and external) is implicit. We believe that the origin of the kinetic barrier that prevents fast interconversion between ${}^3\text{MLCTz}$ and ${}^3\text{MLCTxy}$ is strongly related to this reorganization energy. High-level theoretical calculations could certainly provide key insights into this matter by, for example, helping to identify minima of different electronic configurations in the ${}^3\text{MLCT}$

potential energy surface (44), on one hand, and which nuclear coordinates are involved in the transition between them, on the other hand. These are, however, beyond the scope of the present study. Although further investigations are required to confirm our hypothesis, we postulate that it is the interplay between wave function symmetry-directed orbital overlap and reorganization energy that determines the existence of kinetic barriers between excited states.

Conclusions

In RuRuCr and RuCr⁻, wave function symmetry determines the trajectory undertaken by photoexcited MLCT population. While ³MLCT_z follows an energy transfer pathway, ³MLCT_{xy} proceeds through a back-electron transfer trajectory (Fig. 4 and *SI Appendix*, Fig. S9).

Fundamental to these observations is the spectroscopic handle provided by the PIIVCT band in the NIR transient spectra of photoexcited RuRuCr, which is state-specific and therefore enables us to resolve the fate of the different excited states. Also crucial is that the coexisting ³MLCT excited states have different wave function symmetry, which leads to differential orbital overlap within each state. Consequently, the positive charge density distribution involves different molecular fragments in both coexisting ³MLCTs. This is associated with a reorganization energy for their interconversion and a poor electronic coupling between them. The outcome is a kinetic barrier that potentially allows for trapping high-energy intermediate states, prior to dissipative internal conversion to the lowest ³MLCT. This kinetic barrier can be exploited to catalyze high-energy demanding reactions or to avoid photoinduced oxidative/reductive power losses in energy conversion schemes. Our observations prove the concept that it is possible to drive the excited state population within a molecular chromophore toward different reaction pathways by engineering the excited state wave function symmetries. This is a first step toward a comprehensive manipulation of excited state manifolds of molecular chromophores. Further steps include identifying and synthetically tailoring the electronic factors governing the interconversion barriers between the different excited states and, ultimately, controlling the relative population of the different excited states.

Importantly, RuRuCr and RuCr⁻ are excellent models for complex biological systems, where energy or electron transfer, or in a more general sense, any reactivity of a single molecular species, are controlled by, for example, conformational changes.

Similar mechanisms, based on differential wave function overlap and coupling, might also be involved in natural photosynthesis, with the effect of avoiding dissipation. However, to the best of our knowledge, clear state-specific spectroscopic handles are yet unknown.

Materials and Methods

RuRuCr and RuCr(TPP) (TPP, tetraphenylphosphonium) were available from previous studies (23, 39). Anhydrous DMSO and ACN were provided by Sigma Aldrich and used as supplied. Aqueous solutions of RuCr⁻ were prepared by dissolving it in DMSO and adding water until the DMSO/water ratio was higher than 20:80.

UV-visible spectra were recorded with a Hewlett-Packard 8453 diode array spectrometer in the range 190 to 1,100 nm. All the spectroelectrochemical experiments were performed using a three-electrode optically transparent thin layer electrochemical cell (45, 46), with millimolar solutions of the compounds using [TBA]PF₆ 0.1 M as the supporting electrolyte. Photolysis studies were performed following a previously reported procedure (47) using a 450-nm illumination LED source. Ultrafast transient absorption (TA) experiments were conducted using an amplified Ti:sapphire fs laser system (Clark MXR CPA2101 and 2110, 1 kHz, full width at half the maximum = 150 fs, λ_{exc} = 387 and 505 nm, 200 to 300 nJ per pulse) with TA pump/probe Helios and EOS detection systems from Ultrafast Systems. For the picosecond to nanosecond experiments (Helios), white light was generated focusing a fraction of the fundamental 775-nm output onto a 2-mm sapphire disk (~430 30s760 nm) or a 1-cm sapphire disk (~800 to 1,600 nm). A magic angle configuration was employed to avoid rotational dynamics. Excitation pulses of 387 and 505 nm wavelength were generated by a non-collinear optical parametric amplifier. Band pass filters with ±5 or ±10 nm were used to ensure low spectral width and to exclude 775-nm photons. For the nanosecond to microsecond experiments (EOS), white light (~370 to >1,600 nm) was generated by a built-in photonic crystal fiber super-continuum laser source with a fundamental of 1,064 nm at 2 kHz output frequency and pulse width of ~1 ns. All measurements were conducted in a 2-mm quartz cuvette under argon atmosphere. Obtained data were treated by global and target analyses using the R package TIMP and GloTarAn (24–26).

Data Availability. All study data are included in the article and *SI Appendix*.

ACKNOWLEDGMENTS. This work was supported by grants from the University of Buenos Aires (UBACyT 20020130100534BA), CONICET (PIP 112-20150100394CO), and ANPcyT (PICT 2013 00069 and PICT 2018-00924). A.C. gratefully acknowledges Prof. Dirk Guldí for providing access to ultrafast spectroscopy facilities and continuous support. L.M.B. and A.C. are members of the research staff of CONICET. A.C. is an ALN fellow.

1. R. Hoffmann, R. B. Woodward, The conservation of orbital symmetry. *Acc. Chem. Res.* **1**, 17–22 (1968).
2. R. B. Woodward, R. Hoffmann, The conservation of orbital symmetry. *Angew. Chem. Int. Ed. Engl.* **8**, 781–853 (1969).
3. D. R. Eaton, Selection rules for the isomerization and substitution reactions of transition metal complexes. *J. Am. Chem. Soc.* **90**, 4272–4275 (1968).
4. Y. Zeng, M. B. Zimmt, Symmetry effects in photoinduced electron transfer reactions. *J. Am. Chem. Soc.* **113**, 5107–5109 (1991).
5. K. Kumar *et al.*, Electronic coupling in C-Clamp-Shaped Molecules: Solvent-mediated superexchange pathways. *J. Am. Chem. Soc.* **118**, 243–244 (1996).
6. M. N. Paddon-Row, Some aspects of orbital interactions through bonds: Physical and chemical consequences. *Acc. Chem. Res.* **15**, 245–251 (1982).
7. M. N. Paddon-Row, M. J. Shephard, Through-bond orbital coupling, the parity rule, and the design of “superbridges” which exhibit greatly enhanced electronic coupling: A natural bond orbital analysis. *J. Am. Chem. Soc.* **7863**, 5355–5365 (1997).
8. G. A. Jones, M. N. Paddon-Row, B. K. Carpenter, P. Piotrowiak, Symmetry-forbidden vs symmetry-allowed electron and hole transfer in medium sized intramolecular organic donor-acceptor radical ions. A trajectory surface hopping study. *J. Phys. Chem. A* **106**, 5011–5021 (2002).
9. A. M. Oliver, M. N. Paddon-Row, J. Kroon, J. W. Verhoeven, Orbital symmetry effects on intramolecular charge recombination. *Chem. Phys. Lett.* **191**, 371–377 (1992).
10. M. N. Paddon-Row, Investigating long-range electron-transfer processes with rigid, covalently linked donor-(norbornyllogous bridge)-acceptor systems. *Acc. Chem. Res.* **27**, 18–25 (1994).
11. L. A. Abriata *et al.*, Alternative ground states enable pathway switching in biological electron transfer. *Proc. Natl. Acad. Sci. U.S.A.* **109**, 17348–17353 (2012).
12. F. Blobner *et al.*, Orbital-symmetry-dependent electron transfer through molecules assembled on metal substrates. *J. Phys. Chem. Lett.* **3**, 436–440 (2012).
13. L. Karki, J. T. Hupp, Orbital specific charge transfer distances, solvent reorganization energies, and electronic coupling energies: Electronic Stark effect studies of parallel and orthogonal intervalence transfer in (NO)₅O_s(II)-CN- Ru(III)(NH₃)₅-. *J. Am. Chem. Soc.* **119**, 4070–4073 (1997).
14. T. E. Knight, J. K. McCusker, Orbital-specific energy transfer. *J. Am. Chem. Soc.* **132**, 2208–2221 (2010).
15. S. S. Skourtis, C. Liu, P. Antoniou, A. M. Virshup, D. N. Beratan, Dexter energy transfer pathways. *Proc. Natl. Acad. Sci. U.S.A.* **113**, 8115–8120 (2016).
16. N. F. Polizzi, T. Jiang, D. N. Beratan, M. J. Therien, Engineering opposite electronic polarization of singlet and triplet states increases the yield of high-energy photo-products. *Proc. Natl. Acad. Sci. U.S.A.* **116**, 14465–14470 (2019).
17. P. S. Oviedo, G. E. Pieslinger, L. M. Baraldo, A. Cadranell, D. M. Guldí, Coexistence of MLCT excited states of different symmetry upon photoexcitation of a single molecular species. *J. Phys. Chem. C* **123**, 3285–3291 (2019).
18. Y.-Y. Yang *et al.*, Different degrees of electron delocalization in mixed valence Ru-Ru-Ru compounds by cyanido-/isocyanido-bridge isomerism. *Angew. Chem. Int. Ed. Engl.* **57**, 14046–14050 (2018).
19. L.-T. Zhang *et al.*, Influence of ligand substitution at the donor and acceptor center on MMCT in a cyanide-bridged mixed-valence system. *Dalton Trans.* **48**, 7809–7816 (2019).
20. K. S. Kisel *et al.*, Supramolecular construction of cyanide-bridged Re^I diimine multichromophores. *Inorg. Chem.* **58**, 1988–2000 (2019).
21. D. H. Son, P. Kambhampati, T. W. Kee, P. F. Barbara, Femtosecond multicolor pump-probe study of ultrafast electron transfer of (NH₃)₅Ru(II)NCr(III)(CN)₅- in aqueous solution. *J. Phys. Chem. A* **106**, 4591–4597 (2002).
22. J. F. Endicott, Y. J. Chen, Electronic coupling between metal ions in cyanide-bridged ground state and excited state mixed valence complexes. *Coord. Chem. Rev.* **257**, 1676–1698 (2013).

23. A. Cadranel *et al.*, Distant ultrafast energy transfer in a trimetallic Ru-Ru-Cr complex facilitated by hole delocalization. *Phys. Chem. Chem. Phys.* **19**, 2882–2893 (2017).
24. J. J. Snellenburg, S. P. Laptanok, R. Seger, K. M. Mullen, I. H. M. van Stokkum, Glotaran: A Java -based graphical user interface for the R package TIMP. *J. Stat. Softw.* **49**, (2012).
25. K. M. Mullen, I. H. M. van Stokkum, TIMP: An R package for modeling multi-way spectroscopic measurements. *J. Stat. Softw.* **18**, 46 (2007).
26. I. H. M. Van Stokkum, D. S. Larsen, R. Van Grondelle, Global and target analysis of time-resolved spectra. *Biochim. Biophys. Acta* **1657**, 82–104 (2004).
27. A. Cadranel *et al.*, Electronic energy transduction from Ru(py)₄ chromophores to Cr(III) luminophores. *Inorg. Chem.* **57**, 3042–3053 (2018).
28. M. T. Indelli, F. Scandola, Excited-state charge recombination in a Ru(II)-Cr(III) polynuclear complex. *J. Phys. Chem.* **97**, 3328–3332 (1993).
29. C. A. Bignozzi *et al.*, Intramolecular energy transfer in ruthenium(II)-chromium(III) chromophore-luminophore complexes. Ru(bpy)₂[Cr(cyclam)(CN)₂]₂⁴⁺. *Inorg. Chem.* **31**, 172–177 (1992).
30. B. M. Aramburu-Trošelj, P. S. Oviedo, I. Ramirez-Wierzbicki, L. M. Baraldo, A. Cadranel, Inversion of donor-acceptor roles in photoinduced intervalence charge transfers. *Chem. Commun. (Camb.)* **55**, 7659–7662 (2019).
31. B. M. Aramburu-Trošelj *et al.*, A hole delocalization strategy: Photoinduced mixed-valence MLCT states featuring extended lifetimes. *Inorg. Chem.* **58**, 10898–10904 (2019).
32. N. H. Damrauer *et al.*, Femtosecond dynamics of excited-state evolution in. *Science* **275**, 54–57 (1997).
33. A. Cadranel *et al.*, Spectroscopic signatures of ligand field states in Ru(II)(imine) complexes. *Dalton Trans.* **45**, 5464–5475 (2016).
34. F. Castelli, L. S. Forster, Multiple decays of Cr(CN)₆³⁻ emission in rigid glass solutions. *J. Am. Chem. Soc.* **95**, 7223–7226 (1973).
35. N. Sabbatini, M. A. Scandola, V. Balzani, M. A. Scandola, Intersystem crossing efficiency in the hexacyanochromate(III) ion. *J. Phys. Chem.* **78**, 541–543 (1974).
36. C. A. Bignozzi, M. T. Indelli, F. Scandola, bis(2,2'-bipyridine)ruthenium(II)-hexacyanochromate (III) chromophore-luminophore complexes. Intramolecular energy transfer, excited-state intervalence transfer, and doublet-doublet annihilation. *J. Am. Chem. Soc.* **111**, 5192–5198 (1989).
37. J. T. Hewitt, J. J. Concepcion, N. H. Damrauer, Inverse kinetic isotope effect in the excited-state relaxation of a Ru(II)-aquo complex: Revealing the impact of hydrogen-bond dynamics on nonradiative decay. *J. Am. Chem. Soc.* **135**, 12500–12503 (2013).
38. B. M. Aramburu-Trošelj *et al.*, Wave-function symmetry control of electron-transfer pathways within a charge-transfer chromophore. *J. Phys. Chem. Lett.* **11**, 8399–8405 (2020).
39. A. Cadranel, P. Alborés, S. Yamazaki, V. D. Kleiman, L. M. Baraldo, Efficient energy transfer via the cyanide bridge in dinuclear complexes containing Ru(II) polypyridine moieties. *Dalton Trans.* **41**, 5343–5350 (2012).
40. B. Siewert *et al.*, Turning on the red phosphorescence of a [Ru(tpy)(bpy)(Cl)]Cl complex by amide substitution: Self-aggregation, toxicity, and cellular localization of an emissive ruthenium-based amphiphile. *Chem. Commun. (Camb.)* **53**, 11126–11129 (2017).
41. D. L. Dexter, A theory of sensitized luminescence in solids. *J. Chem. Phys.* **21**, 836 (1953).
42. J. J. Alexander, H. B. Gray, Electronic structures of hexacyanometalate complexes. *J. Am. Chem. Soc.* **90**, 4260–4271 (1968).
43. T. Förster, 10th Spiers Memorial Lecture. Transfer mechanisms of electronic excitation. *Faraday Discuss.* **27**, 7–17 (1959).
44. M. Röhrs, D. Escudero, Multiple anti-Kasha emissions in transition-metal complexes. *J. Phys. Chem. Lett.* **10**, 5798–5804 (2019).
45. W. Kaim, J. Fiedler, Spectroelectrochemistry: The best of two worlds. *Chem. Soc. Rev.* **38**, 3373–3382 (2009).
46. M. Krejčík, M. Daněk, F. Hartl, Simple construction of an infrared optically transparent thin-layer electrochemical cell. *J. Electroanal. Chem. Interfacial Electrochem.* **317**, 179–187 (1991).
47. J. P. Marcolongo, J. Schmidt, N. Levin, L. D. Slep, A chemometric approach for determining the reaction quantum yields in consecutive photochemical processes. *Phys. Chem. Chem. Phys.* **19**, 21373–21381 (2017).